Single-Phase Growth, Stabilization, and Electrical Properties of B Phase VO 2 Films Grown on Mica by Reactive Magnetron Sputtering

E. Ekström, S. Hurand, M. Yildizhan, A. Elsukova, P. Persson, B. Paul, G. Ramanath, A. Le Febvrier, F. Eriksson, P. Eklund

ADVANCED PHYSICS RESEARCH Open Access
www.advphysicsres.com

Single-Phase Growth, Stabilization, and Electrical Properties of B Phase VO_2 Films Grown on Mica by Reactive Magnetron Sputtering

E. Ekström, S. Hurand, M. M. Yildizhan, A. Elsukova, P. O. Å. Persson, B. Paul, G. Ramanath, A. le Febvrier,* F. Eriksson,* and P. Eklund**

The VO_2 metastable (B) phase is of interest for applications in temperature sensing, bolometry, and Li-ion batteries. However, single-phase growth of thin films of this metastable phase is a challenge because vanadium oxide exhibits many polymorphs and the VO_2 stable (M1) phase is usually present as a secondary phase. Additionally, the phase transition at 350 °C in the (B) phase severely narrows the processing window for achieving phase-pure films. Here, single-phase growth of 5-to 50-nm thick VO_2 (B) films on muscovite, mica, by pulsed direct-current reactive magnetron sputtering at 400 °C is demonstrated. The films are phase-pure and exhibit a high density of 4.05 g cm^{-3} and low resistivity of about 50 mΩcm at 30 °C. Increasing the film thickness to 100 nm results in a V_2O_5-capped VO_2 (B) film with a resistivity of 8000 mΩcm. These results indicate that the stability of the VO_2 (B) phase is sensitive to in situ annealing during deposition. These findings should serve as a basis to design processes to exclusively obtain phase-pure VO_2 (B) films.

The presence of numerous phases (e.g., VO, V_2O_3, VO_2 and V_2O_5) and their polymorphs make vanadium oxide attractive for a variety of applications including thermochromic coatings, batteries, and bolometry, to name a few.[1–9] For example, VO_2 has a multitude of polymorphs (e.g., (M1), (M2), (B), (R) and (A)) that can be stabilized by doping, stresses and other means.[10–13] The most studied polymorphs among these are the rutile (R) ($a = b = 4.55$ Å and $c = 2.86$ Å) and monoclinic (M1) ($a = 5.38$ Å, $b = 4.52$ Å, $c = 5.74$ Å and $\beta = 122.6°$) phase, which are the stable phases close to room temperature and exhibit a metal-to-insulator transition at 68 °C.[14] The (A) and (B) phase are also tetragonal ($a = b = 8.43$ Å and $c = 7.68$ Å) and monoclinic ($a = 12.03$ Å, $b = 3.69$ Å, $c = 6.42$ Å and $\beta = 106.6°$), respectively. It is known that small changes in growth parameters, such as temperature and oxygen partial pressure, can be utilized for selectively grow different phases and polymorphs. The V-V distance seems to be the key parameter to which polymorph is formed.[15] Additionally, the choice of substrate plays a role in the growth mode and formed phases. We have previously shown that VO_2 (M1) phase can be grown by van der Waals epitaxy on mica.[16] In general, growth on mica may be by van der Waals epitaxy or conventional epitaxy, and it is thus important to prove all features of van der Waals epitaxy, rather than assuming it, as is sometimes done in the literature. There is also a recent report of a third type of epitaxy on mica, substrate-compliant epitaxy.[17] In contrast, the (B) phase can be grown by changing the partial pressure of oxygen, as will be shown in the present paper. Mica is also a flexible substrate, allowing for applications where flexible devices are needed.[18,19]

The (B) phase, which is of potential use in Li-ion batteries, has promising electrical properties and can detect small increases in temperatures. The latter is of importance in such diverse areas as bolometers, temperature management in microsystems and precise temperature sensing. It is also of potential use in optical sensors. While these features provide versatility in properties and applications, exclusive synthesis of desired phase(s) is a challenge. Hydrothermal methods allows growth of B-phase nanostructures such as nanorods, but phase-pure growth of epitaxial films or single crystals is challenging, For instance, although the metastable (B) phase (space group C2/m) can be stabilized by stress, its exclusive growth is constrained by its conversion to the stable rutile

E. Ekström, M. M. Yildizhan, A. Elsukova, P. O. Å. Persson, B. Paul, A. le Febvrier, F. Eriksson, P. Eklund
Thin Film Physics Division
Department of Physics
Chemistry and Biology (IFM)
Linköping University
Linköping SE-581 83, Sweden
E-mail: erik.ekstrom@ri.se; arnaud.le.febvrier@liu.se; fredrik.eriksson@liu.se; per.eklund@liu.se

S. Hurand
Institut Prime
Université de Poitiers
11 Boulevard Marie et Pierre Curie, Chasseneuil du Poitou 86360, France

G. Ramanath
Department of Materials Science and Engineering
Rensselaer Polytechnic Institute
Troy, NY 12180, USA

The ORCID identification number(s) for the author(s) of this article can be found under https://doi.org/10.1002/apxr.202300032

DOI: 10.1002/apxr.202300032

(R) phase at 350 °C.[20] While pulsed laser deposition has demonstrated the growth of the (B) phase at higher temperatures,[21,14] the (M1) phase is also usually present in these films.[22,23] Hence, there are continued efforts to devise new methods to grow phase-pure films of the VO_2 (B) phase at a sufficiently high temperature to obtain good film quality, without activating the B-to-R phase transition.

Here, we demonstrate single-phase growth of 5- to 50-nm thick films VO_2 (B) films on muscovite mica substrates by pulsed DC (direct current) reactive magnetron sputtering at 400 °C. These phase-pure films exhibit a low resistivity of 50 mΩcm at 30 °C. Increasing the film thickness to 100 nm results in a V_2O_5-capped VO_2 (B) film with a resistivity of 8000 mΩcm. These results indicate that the stability of B-phase VO_2 is sensitive to in situ annealing during deposition. Our findings should serve as a basis to design processes to exclusively obtain phase-pure VO_2 (B) films.

The VO_2 films were grown on freshly tape-cleaved muscovite mica (001) substrates obtained from Oxford Instruments using pulsed DC reactive magnetron sputtering. A 99.7% pure 2-inch vanadium target (Plasmaterials, Livermore, CA, USA) was sputtered using an 89:11 Ar-O_2 mixture at 0.53 Pa (4 mTorr). Prior to deposition, the substrates were heated to 400 °C, and held for 10 min for degassing at a 6.7×10^{-6} Pa (5×10^{-8} Torr) base pressure. The chamber is described elsewhere.[24] The substrate temperature was maintained at 400 °C throughout the deposition. For the depositions, a 160 W power source was pulsed at 50 Hz, at a 90% duty cycle, a 30 μs crowbar length, and a 10% reversed voltage with a floating substrate bias. Film thickness t_{film} measured by x-ray reflectivity (XRR) [see Figure S1, Supporting Information] revealed that the planar growth rate of the films was 1 nm per min. Accordingly, the deposition time was varied from 5 to 100 mins to obtain films with 5 nm ≤ t_{film} ≤ 100 nm.

X-ray diffractometry (XRD) was performed using a X"Pert PRO powder diffractometer with a copper anode source (Cu Kα, λ = 1.54 Å), operated at 45 kV and 40 mA. The incident beam path included a 0.5° divergence slit followed by Bragg-Brentano^{HD} optical module and a 0.5° anti-scatter slit. The diffracted beam path comprised of a 5 mm anti-scatter slit followed by a 0.04 rad Soller slit, and a Ni-filter. An X"Celerator detector operated in scanning line mode with a 2.122° active length was used to quantify the diffracted X-rays. XRR measurements to determine the film thickness and density were carried out in a PANalytical Empyrean diffractometer with a copper anode source (Cu Kα, λ = 1.54 Å), operated at 45 kV and 40 mA. The incident beam path consisted of a 1/32° divergence slit and a hybrid mirror, and in the diffracted beam path a triple axis Ge 220 analyzer was used together with a PIXcel3D detector operated in open detector mode.

A LEO Gemini 1550 Zeiss instrument was used for scanning electron microscopy (SEM) of the film surfaces. A Carl Zeiss crossbeam 1540 Focused Ion Beam system was used to prepare samples for transmission electron microscopy (TEM) for which a 200 kV FEI Tecnai G2 instrument or the Linköping monochromated, double-corrected 300 kV FEI Titan^3 60–300 (S)TEM were employed. Electron energy loss spectroscopy was carried out with a 0.2 eV energy resolution using a Gatan GIF Quantum ERS post-column energy filter.

Room-temperature electrical resistivity of the films were determined from four-point probe measurements in a Jandel RM3000 instrument together with XRR-determined film thicknesses. The temperature dependence of the resistivity from 30 °C to 120 °C was measured in a four-probe van der Pauw configuration with an input current of 10 μA on the high-temperature module AHT55T5 of a Hall Measurement System HMS-5300 provided by the ECOPIA company.

SEM images from the as-deposited film with thickness t_{film} = 5 nm and t_{film} = 10 nm (see **Figure 1**a) shows no detectable topographical contrast from grains or surface features and suggest sub-nm surface roughness. Films with t_{film} = 21 nm and t_{film} = 50 nm reveal mild contrast indicating 100–200 nm grains (see Figure 1b). Films with t_{film} = 100 nm (see Figure 1c) exhibit distinct contrast arising from randomly oriented faceted grains.

X-ray diffractograms (**Figure 2**a) reveal a strong 001 peak, whose width w_{001} decreases with increasing film thickness (Figure 2b). Thickness fringes are visible around the 001 peak for t_{film} = 21 nm and t_{film} = 50 nm, indicating good crystal quality. For films with $t_{film} \leq 50$ nm, the 001 peak shifts to higher angles with increasing film thickness, attributable to the variation of film stress with film thickness.[25,26] Diffractograms from 100 nm thick films exhibit additional peaks from a secondary phase corresponding to the 001 and 102 Bragg reflections from the V_2O_5 structure.

Film density analysis from XRR data (see Figure S1, Supporting Information) indicates that the surface of the 100 nm thick film has a lower density of 3 g cm^{-3} as compared to 4 g cm^{-3} for the $t_{film} \leq 50$ nm films. We propose, given that V_2O_5 has a lower density than VO_2 (B) and the fact that 100 nm thick films exhibit underdense surface morphology with randomly oriented faceted grains, that the surface of the 100 nm thick films consists of the V_2O_5 phase. Thus, the higher density films with $t_{film} \leq 50$ nm consist exclusively of phase-pure VO_2 (B) films, consistent with featureless SEM images. These results suggest that at extended deposition times, the VO_2 (B) formation gives way to V_2O_5 formation, underscoring the delicate balance between kinetic, thermodynamic, and other factors such as possible strain, that determine phase selection in this system.

TEM micrographs from cross-sections of films with t_{film} = 50 nm indicate a continuous and uniform film (see **Figure 3**a) with high crystallinity (Figure 3b) throughout the film thickness. The film thickness is determined to be ≈50 nm throughout the entire lamella. A lattice resolved image of the sample is illustrated in Figure 3c and a Fast Fourier Transform (FFT) obtained from the same region, provided in the inset, reveal the main reflections. The pattern is in good agreement with $(1\bar{1}0)$ projection of VO_2 –(B) [ICDD PDF 01-081-2392].

High angle annular dark field scanning TEM (HAADF-STEM) images from films with t_{film} = 100 nm revealed a layered film microstructure (**Figures 4**a, **5**a). The chemical structure of the film layers was identified using near edge fine structure of the electron energy loss (EEL) spectra[27] to chemically distinguish the VO_2 and V_2O_5 regions. This approach circumvents the complication of overlapping V L and O K edges in both EDX and EEL spectra for these phases. EEL spectra acquired from various film layers were compared with reference spectra from the vanadium oxide VO_2 and V_2O_5 phases.[14] The difference in near-edge fine structures of the two phases is manifested by the presence of a shoulder in the VO_2 spectrum (marked by a red arrow in Figure 4c), shapes of the oxygen O-K(P) and O-K(Q) peaks and their ratio to the vanadium $L_{2,3}$ edges. The vanadium oxidation states were

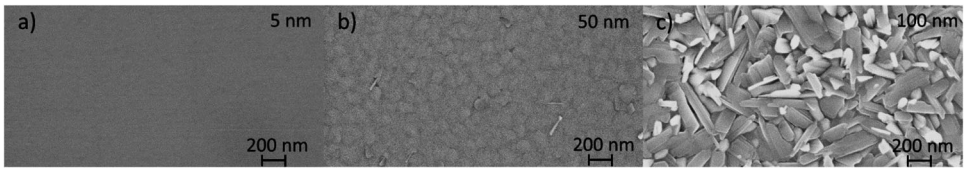

Figure 1. SEM images from VO_2 films with a) t_{film} = 5 nm, b) t_{film} = 50 nm, and c) t_{film} = 100 nm.

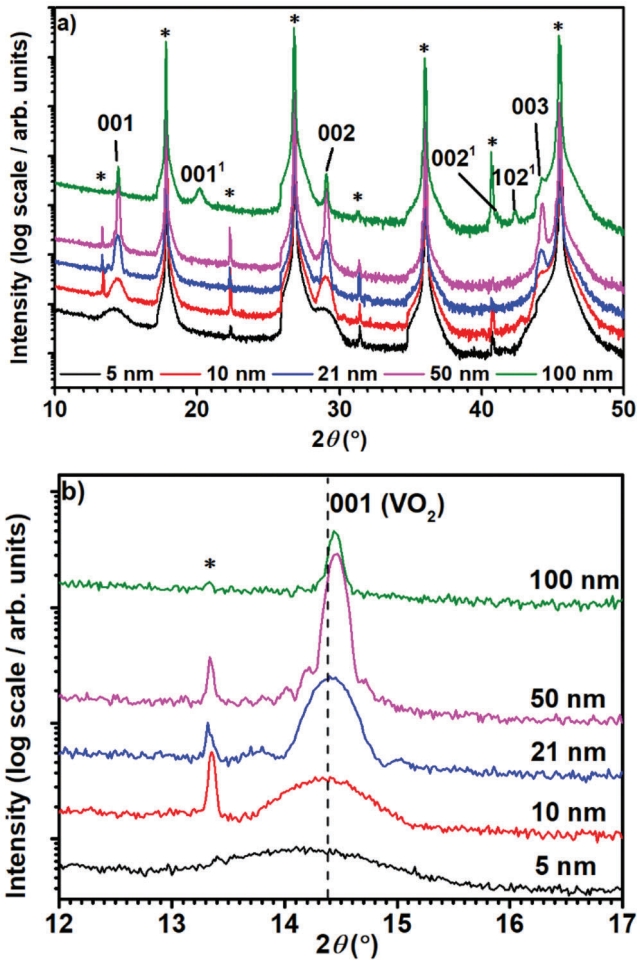

Figure 2. 2θ–θ X-ray diffractograms of the VO_2 films are shown in (a) and zoomed in diffractogram of the 001 film peak is shown in (b), highlighting the peak shift to higher diffraction angles for thicker films. Substrate peaks are marked by an asterisk, while indexed peaks correspond to the V_2O_5 structure.

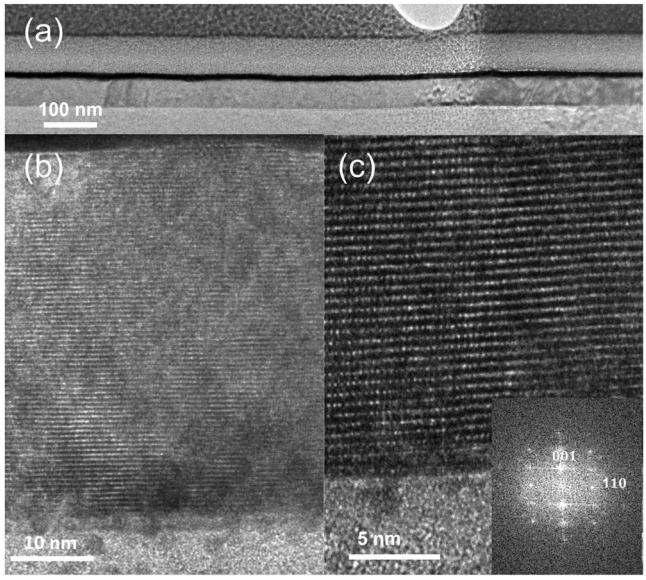

Figure 3. Cross-section TEM micrographs from a film with t_{film} = 50 nm. a) Low magnification overview, b) high magnification of the film thickness and c) lattice resolved micrograph of the same film. The FFT obtained from (c) is shown in the inset.

mapped by fitting experimental spectrum derivatives with a linear combination of the derivatives of VO_2 and V_2O_5 reference spectra (Figure 4d). The map shows that the bottom layer exhibits a VO_2 oxidation state, and the upper layers are composed either of V_2O_5 or a mix of oxides. Another area was analyzed in the same way and shows similar results, see Figure S3 (Supporting Information) for more details.

High resolution HAADF-STEM imaging was used to investigate the crystal structure of the 100 nm film (Figure 5a–c) FFT analysis confirmed the presence of V_2O_5 phase in a middle layer of the film (Figure 5b and insets). However, the FFT pattern of the bottom image layer could not be unequivocally matched to a VO_2 (B) phase (Figure 4c and inset). To further analyze the structure of the bottom layer, we obtained a selected area diffraction pattern calibrated using an oriented gold thin film (Figure 5d,e). Experimental diffraction pattern was matched to all possible vanadium oxide phases. None of the phases matched the obtained diffraction precisely, with phases (B) and (M2) providing the closest matches. In Figure 5e, simulated corresponding diffraction patterns are overlayed with diffraction image. The experimental diffraction spots lie between two reflections from two phases (Figure 5e, inset). This result indicates that during the film growth the bottom layer undergoes an unfinished transition from (B) to (M2) phase.

The electrical resistivity of the VO_2 (B) films does not vary appreciably at ≈50 mΩcm for film thicknesses in the 5 nm ≤ t_{film} ≤ 50 nm range. In comparison, literature reports resistivity values in a wide range, 4 mΩcm – 500 mΩcm.[6,15,16] The film with t_{film} = 100 nm that contained both the VO_2 and V_2O_5 phases exhibited a resistivity of 8000 mΩcm, showing the strong influence of the high resistivity V_2O_5 phase. The resistivity of films with 5 nm ≤ t_{film} ≤ 50 nm decreases with temperature, typical of semimetal behavior expected for the VO_2 (B) around room temperature.[15,16] There are no observable sharp changes in the resistivity between

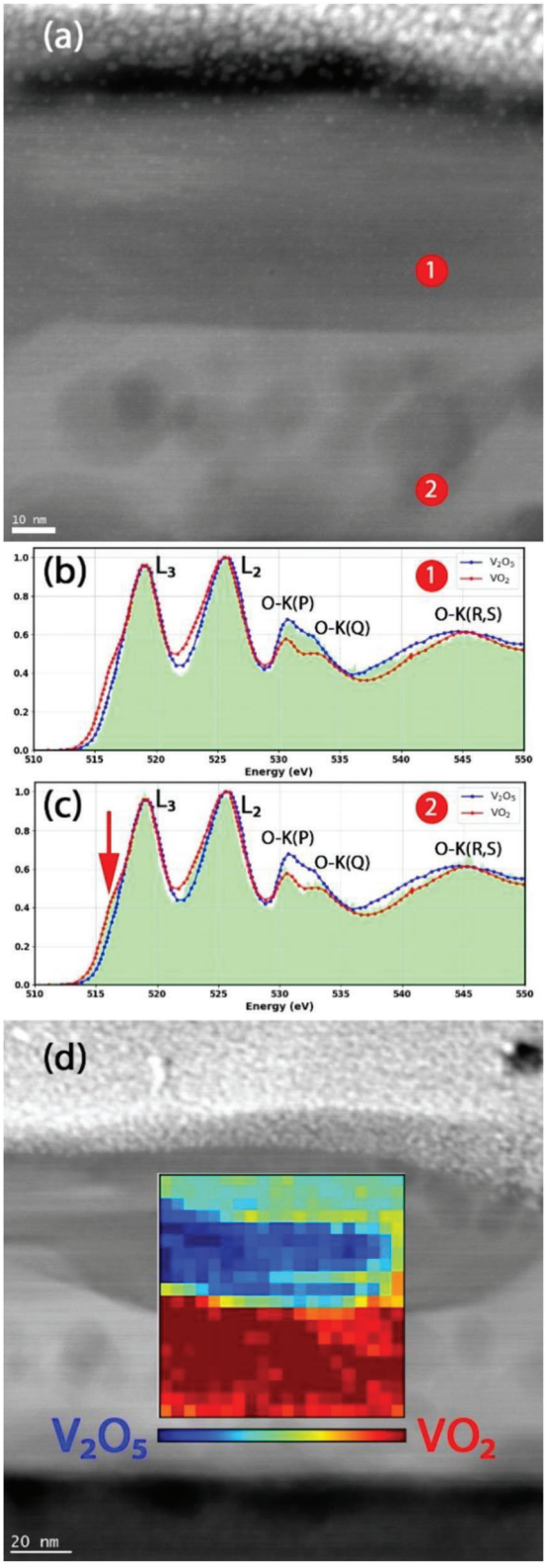

Figure 4. a) HAADF-STEM image of three-layer vanadium oxide thin film. b,c) EEL spectra (green area) obtained from points 1 and 2 marked in image (a) plotted together with reference VO_2 and V_2O_5 spectra (red and blue lines, respectively). d) HAADF-STEM image of three-layer vanadium oxide thin film with corresponding map of vanadium oxidation state.

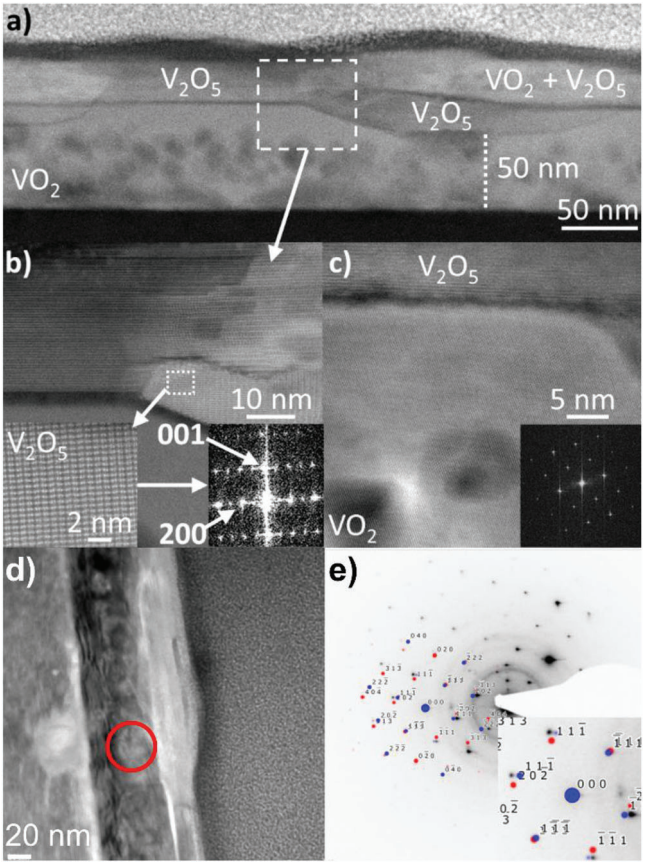

Figure 5. a–c) HAADF-STEM images from a 100 nm thick film. Insets in (b) show high resolution lattice images and a FFT from V_2O_5 in the middle layer, while the inset in (c) indicates the FFT from the VO_2 (B) layer closer to the substrate. d) Overview bright field TEM image of a 100 nm thick film with e) a corresponding selected area diffraction pattern obtained from the area marked with red circle. Simulated diffraction patterns for (B) and (M2) vanadium oxide phases (red and blue dots, respectively) are overlayed on experimental image.

30 °C and 120 °C, indicating unlikelihood of presence of any significant amounts of VO_2 (M1), known to exhibit a metal-insulator transition[17] at 68 °C. These results again are consistent with our XRD and TEM results.

The temperature coefficient of resistance (TCR), α, of the films are calculated by using Equation (1),

$$\frac{\mathrm{d}\rho}{\rho \mathrm{d}T} = \alpha \tag{1}$$

where ρ and T are resistivity and temperature, respectively. The films with thicknesses 10 nm to 50 nm have similar TCR values of $-1.5\%\ K^{-1}$ at 30°C to $-1.0\%\ K^{-1}$ at 120°C. The 5 nm thick film follows the same trend with an overall 0.5 percentage points higher ($-2.0\%\ K^{-1}$ at 30°C to $-1.0\%\ K^{-1}$ at 120°C). These values are slightly lower at low temperatures compared to Kil et al. who reports $-3.5\%\ K^{-1}$ at 25 °C[6] and Wan et al. with $-2\%\ K^{-1}$.[5] However, at higher temperatures our films are comparable to what Kil et al. and Wada et al. report.[6,28] Nevertheless, the low resistivity of the films in this study makes them attractive for reducing

signal noise, making them interesting for bolometric applications even though the TCR is lower.

Some additional findings can be extracted from the temperature-dependent electrical resistivity. The electrical resistivity of VO_2 decreases with temperature, i.e., the films are semiconducting, and the transport properties will be related to the excitation energy or bandgap, ΔE. That means that the electrical resistivity will be an exponential function of ΔE. An Arrhenius plot can be applied to extract the ΔE as shown in **Figure 6**c. With the decrease in film thickness, the slope of the Arrhenius plot varies, resulting in different values of ΔE. In Figure 6c, it is visible that the black line corresponds to the highest slope resulting in a ΔE of 210 meV, which is substantially higher (around 100 meV) than that of the thicker films. This may be due to the increased bandgap or excitation energy ΔE_{5nm} of $t_{film} = 5$ nm due to quantum confinement and/or other subtle changes in microstructure or compositional variations.

The temperature stability of the films was investigated by XRD combined with in situ annealing in air, see Figure S4 (Supporting Information) for more details. The results showed that the VO_2 (B) film is stable up to 350 °C. At 375 °C, the V_2O_5 phase was observed and at 400 °C the film was fully transformed to the new structure. The temperature is in similar range as what Tsang and Manthiram observed on a VO_2 (B) sample in differential scanning calorimetry and thermogravimetric analysis in 1997 (performed in N_2 atmosphere).[14] With the distinct difference that the new phase formed in their study was the thermodynamically stable VO_2 in monoclinic rutile (M1) phase. The different phases formed can be explained in the different atmosphere used. In their study, no extra oxygen was available during annealing and thus the formation of V_2O_5 was not possible. While our annealing was performed in air which allowed the VO_2 film to adsorb more oxygen resulting in the more stable V_2O_5 phase to form. It is conceivable that the formation of other phases and polymorphs of vanadium oxide on mica can be achieved by annealing at different gas ambients and partial pressures during growth (see Figure S5, Supporting Information) or post-deposition annealing.

Conclusions

We have grown 5- to 50-nm thick films of dense metastable VO_2 (B) films of uniform thickness and low surface roughness on mica substrates using pulsed DC magnetron sputtering at relatively high temperatures (400 °C). The phase pure films are semiconducting and exhibit a low resistivity of 50 mΩcm at 30 °C. The electrical transport in these films is strongly dependent on the film thickness in the range $5 \text{ nm} \leq t_{film} \leq 21$ nm as the characteristic activation energy for carrier transport decreases from ΔE = 210 meV to 110 meV with increasing thickness. The activation energy remains unchanged with further increases in thickness, suggesting quantum confinement effects. A secondary V_2O_5 phase can be formed at films thicker than 50 nm, or by subjecting the films to a post-deposition anneal in air above 350 °C. The formation of V_2O_5 can increase the resistivity by more than two orders in magnitude. The identity of the oxides formed through the decomposition of VO_2 (B) during annealing is sensitive to the gas ambient during deposition and post-deposition annealing. Pulsed DC reactive sputtering offers multiple avenues for

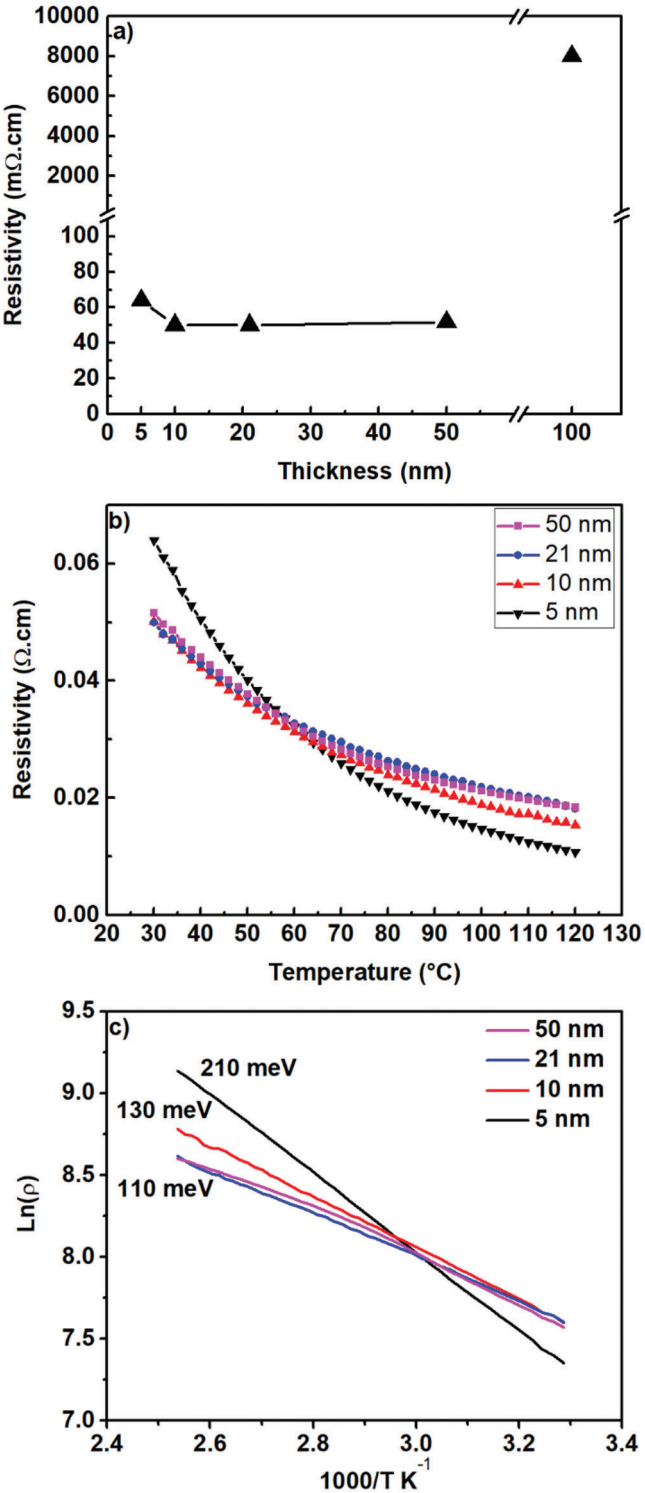

Figure 6. Resistivity versus thickness is shown in (a). In (b), resistivity versus temperature is shown where red, orange, green and blue lines correspond to 5, 10, 21, and 50 nm, respectively. Arrhenius plots of the $t_{film} \leq 50$ nm is shown in (c).

phase selection in vanadium oxide thin films, that may not be accessible through other deposition methods.

Supporting Information

Supporting Information is available from the Wiley Online Library or from the author.

Acknowledgements

The authors acknowledge funding from the Swedish Research Council (VR) under Project No. 2016–03365, the Knut and Alice Wallenberg Foundation through the Wallenberg Academy Fellows program (grant no. KAW 2020.0196), the Swedish Government Strategic Research Area in Materials Science on Functional Materials at Linköping University (Faculty Grant SFO-Mat-LiU No. 2009 00971), and the Swedish Energy Agency under project 46519-1. The authors also acknowledge access to the Swedish National Infrastructure for Advanced Electron Microscopy, ARTEMI, supported by the Swedish Research Council (VR) and The Foundation for Strategic Research (SSF), through grants 2021-00171 and RIF21-0026. S. H. acknowledges the French government program "Investissements d'Avenir" (EUR INTREE, Reference No. ANR-18-EURE-0010, and LABEX INTERACTIFS, Reference No. ANR-11-LABX-0017-01).

Conflict of Interest

The authors declare no conflict of interest.

Data Availability Statement

The data that support the findings of this study are available from the corresponding authors upon reasonable request.

Keywords

alEpitaxy, metastable phases, PVD, Thin film, VO_2

Received: March 18, 2023
Revised: May 7, 2023
Published online: June 3, 2023

[1] S. M. Babulanam, T. S. Eriksson, G. A. Niklasson, C. G. Granqvist, *Solar Energy Materials* **1987**, *16*, 347.
[2] Y. Gao, H. Luo, Z. Zhang, L. Kang, Z. Chen, J. Du, M. Kanehira, C. Cao, *Nano Energy* **2012**, *1*, 221.
[3] H. Liu, Y. Wang, K. Wang, E. Hosono, H. Zhou, *J. Mater. Chem.* **2009**, *19*, 2835.
[4] H. Wang, X. Yi, S. Chen, *Infrared Phys. Technol.* **2006**, *47*, 273.
[5] D. Y. Wan, P. Xiong, L. Chen, S. Shi, A. Ishaq, H. Luo, Y, Gao, *Appl. Surf. Sci.* **2017**, *397*, 30.
[6] T.-H. Kil, H.-J. Choi, G. Lee, B.-H. Lee, S. Y. Jung, R. Ning, C. Park, S. O. Won, H. J. Chang, W. J. Choi, S.-H. Baek, *J. Eur. Ceram. Soc.* **2020**, *40*, 5582.
[7] Z. Cao, S. Li, W. Xie, G. Du, Z. Qiao, *Calphad* **2015**, *51*, 241.
[8] P. Shvets, O. Dikaya, K. Maksimova, A. Goikhman, *J. Raman Spectrosc.* **2019**, *50*, 1226.
[9] S. Surnev, M. G. Ramsey, F. P. Netzer, *Prog. Surf. Sci.* **2003**, *73*, 117.
[10] J. Nag, R. F. Haglund Jr, *J. Phys. Cond. Matter* **2008**, *20*, 264016.
[11] J. Galy, G. Miehe, *Solid State Sci.* **1999**, *1*, 433.
[12] B. L. Chamberland, *J. Solid State Chem.* **1973**, *7*, 377.
[13] C. R. A. Catlow, A. N. Cormack, F. Théobald, *Acta Crystallogr. Sect. B-Struct. Commun.* **1984**, *40*, 195.
[14] S. Lee, I. N. Ivanov, J. K. Keum, H. N. Lee, *Sci. Rep.* **2016**, *6*, 19621.
[15] A. Srivastava, H. Rotella, S. Saha, B. Pal, G. Kalon, S. Mathew, M. Motapothula, M. Dykas, P. Yang, E. Okunishi, D. D. Sarma, T. Venkatesan, *APL Mater.* **2015**, *3*, 026101.
[16] E. Ekström, S. Hurand, A. le Febvrier, A. Elsukova, P. O. Å. Persson, B. Paul, F. Eriksson, G. Sharma, O. Voznyy, D. G. Sangiovanni, G. Ramanath, P. Eklund, *Mater. Des.* **2023**, *229*, 111864.
[17] N. Wang, X. Pan, P. Wang, Y. Wang, H. He, Y.-J. Zeng, L. Zhang, Y. Li, F. Wang, B. Lu, J. Huang, Z. Ye, *Mater Today Bio* **2022**, *20*, 100255.
[18] L. A. Walsh, C. L. Hinkle, *Appl. Mater. Today* **2017**, *9*, 504.
[19] Y.-H. Chu, *npj Quantum Mater.* **2017**, *2*, 67.
[20] C. Tsang, A. Manthiram, *J. Electrochem. Soc.* **1997**, *144*, 520.
[21] A. Srivastava, H. Rotella, S. Saha, B. Pal, G. Kalon, S. Mathew, M. Motapothula, M. Dykas, P. Yang, E. Okunishi, D. D. Sarma, T. Venkatesan, *APL Mater.* **2015**, *3*, 026101.
[22] A. Chen, Z. Bi, W. Zhang, J. Jian, Q. Jia, H. Wang, *Appl. Phys. Lett.* **2014**, *104*, 071909.
[23] N. Emond, B. Torriss, M. Chaker, *Sci. Rep.* **2018**, *8*, 7153.
[24] A. le Febvrier, L. Landälv, T. Liersch, D. Sandmark, P. Sandström, P. Eklund, *Vacuum* **2021**, *187*, 110137.
[25] V. Ion, F. Craciun, N. D. Scarisoreanu, A. Moldovan, A. Andrei, R. Birjega, C. Ghica, F. Di Pietrantonio, D. Cannata, M. Benetti, M. Dinescu, *Sci. Rep.* **2018**, *8*, 2056.
[26] H. Paik, J. A. Moyer, T. Spila, J. W. Tashman, J. A. Mundy, E. Freeman, N. Shukla, J. M. Lapano, R. Engel-Herbert, W. Zander, J. Schubert, D. A. Muller, S. Datta, P. Schiffer, D. G. Schlom, *Appl. Phys. Lett.* **2015**, *107*, 163101.
[27] S. Kalavathi, S. Amirthapandian, S. Chandra, P. C. Sahu, H. K. Sahu, *Journal of physics. Condensed matter* **2014**, *26*, 015601.
[28] H. Wada, M. Nagashima, N. Oda, T. Sasaki, A. Kawahara, M. Kanzaki, Y. Tsuruta, T. Mori, S. Matsumoto, T. Shima, M. Hijikawa, N. Tsukamoto, H. Gotoh, *Design and performance of 256x256 bolometer-type uncooled infrared detector*, Vol. *3379*, SI (SPIE, 1998).